npj | climate and atmospheric science

www.nature.com/npjclimatsci

ARTICLE OPEN

Check for updates

Enhancement of Indian summer monsoon rainfall by cross-equatorial dry intrusions

Deepika Rai[1]✉ and Shira Raveh-Rubin[1]✉

The Indian summer monsoon affects the lives of over 1/6 of the world's population. Precipitation extremes during summer monsoons have dire socioeconomic impacts. Yet, the mechanisms leading to these extremes are poorly understood, making their accurate forecasts and reliable future projections a longstanding challenge. Using a Lagrangian-based method, we show that precipitation extremes link to dry air intrusions from the southern midlatitudes upper troposphere, crossing the equator, and reaching the Arabian Sea. By triggering intense ocean evaporation, these dry intrusions are associated with modulated moisture transport patterns toward India and enhanced precipitation by >17% on average, often embedding local extremes. A notable example is the excessive rain that caused the devastating Kerala flood of 2018. However, depending on the wind pattern, these dry intrusions may, in some cases, decrease rainfall over land. The emerging connection of rainfall variability with midlatitude weather systems opens opportunities for improving the forecast of precipitation extremes and understanding their future projections.

npj Climate and Atmospheric Science (2023)6:43 ; https://doi.org/10.1038/s41612-023-00374-7

INTRODUCTION

Typically lasting from June to September (JJAS), the summer monsoon accounts for ~80% of India's annual precipitation[1,2]. Consequently, its impact on India's agriculture and water resources is immense, with any variability in rainfall substantially affecting the country's society and economy[3,4]. The monsoon rainfall is associated with variability across various timescales, from intraseasonal to multi-decadal[5–9]. On year-to-year timescale, seasonal mean rainfall varies by ~10% (standard deviation) from its long-term mean[10,11]. However, the pronounced daily-to-weekly fluctuations can deviate more than 100% from the long-term mean[12]. A substantial precipitation variability on the daily-to-weekly scale is due to active and break phases, also known as wet and dry spells, during which precipitation over the monsoon core exceeds the long-term mean by one standard deviation for at least 3 days[12]. The break phases are less frequent than the active phases but last longer[12]. As such, long breaks are often associated with a poor monsoon or drought[13], while most of the seasonal rainfall occurs during the active phases[14]. Extreme rain events significantly increase the possibility of floods[15,16]. The devastating outcomes of such floods are highlighted by the statewide flood in Kerala during the 2018 summer monsoon, which caused more than 400 deaths and displaced millions of people[15]. More frequent and intense extreme rain episodes are expected under global warming scenarios[10].

The primary source of moisture during the monsoon season is the western Indian Ocean[17], encompassing most of the Arabian Sea and extending up to Madagascar along the coast of East Africa. During the northern summer, the western Indian Ocean is associated with a high-intensity cross-equatorial low-level jet (C-shaped flow between 20°S to 20°N and 40 to 80°E, Fig. 1a). The low-level jet speed, westerly wind depth, zonal water vapor flux, horizontal wind shear, and cyclonic vorticity, all affect the heavy rainfall events over southern peninsular India during the monsoon season[18]. The low-level jet transporting moisture toward India[19] changes its characteristics during active and break phases[20]. Typically, active phases are associated with strong low-level cyclonic circulation over India and the Bay of Bengal and moisture convergence over the monsoon core region, whereas break phases are marked by anticyclonic circulation and moisture divergence[21]. Changes in moisture transport along the low-level jet may thus potentially impact moisture convergence and the rainfall variability downstream[22].

At times, the large influx of moist air through the low-level jet encounters the intrusions of stratospheric/upper-tropospheric dry air from western Asia. This incursion of dry air towards India intensifies dry conditions and limits the monsoon rain by inhibiting the vertical growth of deep convection[22–26]. Moreover, the interaction of mid-level dry air from western and central Asia with the moist low-level flow from the Arabian Sea controls the onset and progression of the monsoon[27,28]. A trajectory-based climatology of dry intrusions (DIs) suggests, however, that such airstreams peak in winter[29]. Thus, more DIs typically initiate in the southern hemisphere during the Indian summer monsoon season[29,30]. While descending slantwise toward lower latitudes, DIs may reach the tropics (hereafter 'tropical DIs') and even cross the equator (hereafter 'cross-equatorial DIs')[29]. Although rare, cross-equatorial DIs (Fig. 2a, b, cyan contour) are indeed more frequent than DIs initiated in the northern hemisphere during the monsoon season[29]. Cross-equatorial DIs can dramatically affect moisture availability during the summer monsoon, especially if they remain in the lower troposphere. It has been proposed that the injection of dry air from the southern midlatitudes into the low-level jet may limit monsoon-related moisture transport and precipitation[31,32]. However, the coherent impact of cross-equatorial DIs on monsoon rainfall remains unclear.

We here present a method that combines objective, Lagrangian-based identification criteria with statistical analysis to quantify and understand the impact of cross-equatorial DIs on the summer monsoon rainfall within the target region (marked in black in Fig. 4). Our findings shed light on the occurrence of cross-equatorial DIs, their effects on the Indian summer monsoon

[1]Department of Earth and Planetary Sciences, Weizmann Institute of Science, Herzl Street 234, Rehovot 7610001, Israel. ✉email: Deepika.rai@weizmann.ac.il; Shira.raveh-rubin@weizmann.ac.il

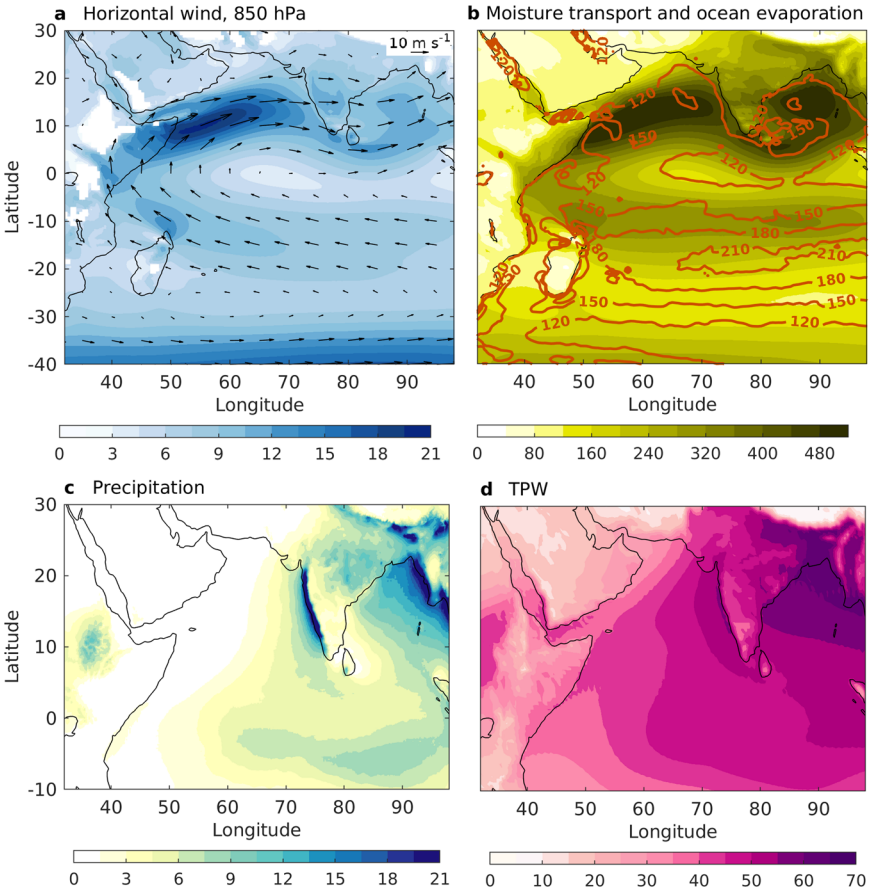

Fig. 1 Seasonal mean during the climatological period (JJAS). a Wind vectors and speed at 850 hPa (m s^{-1}), **b** moisture transport (integrated from surface to 200 hPa, kg m^{-1} s^{-1}, shading) and ocean evaporation (W m^{-2}, orange contours), **c** precipitation (mm day^{-1}), and **d** total precipitable water (TPW, mm).

rainfall, and underlying mechanisms, with implications for rainfall predictability.

RESULTS

Dry Intrusions reaching the Arabian Sea

Based on 40 summer monsoon seasons from 1979 to 2018, globally, tropical DIs originating in the southern hemisphere start the slantwise descent in the extratropics, mostly between 40 and 50°S, with several peak frequencies (>2% of the time in JJAS) in the eastern Atlantic, eastern Pacific, south Indian Ocean, and southeast Australia (Fig. 2a, shading). In this season, there is only a weak signal of tropical DIs initiating in the northern hemisphere, particularly over western and central Asia, with less than 0.2% frequency (not shown). At 120 h after initiation (initiation refers to the start of descent), tropical DI air is mainly found between 15°S and the equator, with a pronounced frequency of above 6% around 12°S and a ubiquitous signature over the Indian Ocean (Fig. 2b, shading). Only in the western Indian Ocean do tropical DIs cross the equator and reach beyond 10°N, with an occurrence frequency above 0.5% (Fig. 2a, b, cyan contours). Such tropical DIs with their origin in the southern hemisphere that cross the equator and reach the northern hemisphere at some point during their lifetime are defined here as cross-equatorial DIs.

More than 15% of the global DIs are labeled as tropical DI, with a peak during July (Fig. 2c, d). Less than 1% of the global DIs fall under the cross-equatorial DI category, with a peak in June (Fig. 2c, e). Of those, cross-equatorial DIs that specifically reach the Arabian Sea (Fig. 2b, dashed black box) within 120 h after initiation are considered Arabian Sea DIs. Although the number of Arabian-Sea DIs is low, they account for more than 35% of the global cross-equatorial DIs and peak in June (Fig. 2c, f). These DIs typically enter the marine boundary layer below 850 hPa over the central Indian Ocean (CIO, black box in Fig. 3d) and the Arabian Sea, where they interact with moisture that feeds the monsoon rainfall.

During the study period, DIs reaching the Arabian Sea are aggregated into 137 unique events, i.e., 3–4 events per year, with maximum 8 events in 1993 but none in 2011. For each event, we define the start time (t_s) as the initiation of a DI over the southern extratropics and the end time (t_e) as the time when it ceases to initiate (see 'Methods'). With these definitions, the impact of DIs on the Indian Ocean is expected to occur during the days following t_e, when DI air descends slantwise northward toward the lower troposphere.

Mechanisms enhancing moisture transport

The low-level jet is vital in transporting moisture toward India during the summer monsoon (Fig. 1). Significant anomalies along the moisture pathways are evident following the DI events (Fig. 3). At t_s, anomalies in moisture and the low-level jet are weak over the Indian Ocean (Fig. 3a), particularly the western Indian Ocean and CIO, as DI air initiates its descent south of 35°S (cyan contour). With the northward propagation and slantwise descent of DI, the upper-tropospheric dry air from higher latitudes in the southern hemisphere reaches the CIO's lower troposphere and modulates its thermodynamic properties, including low-level winds (Fig. 3). It is already known that DIs start their descent in the vicinity of the upper-tropospheric jet[29,33]. Mixing of high-momentum DI air into the lower troposphere is expected to result in the stronger low-

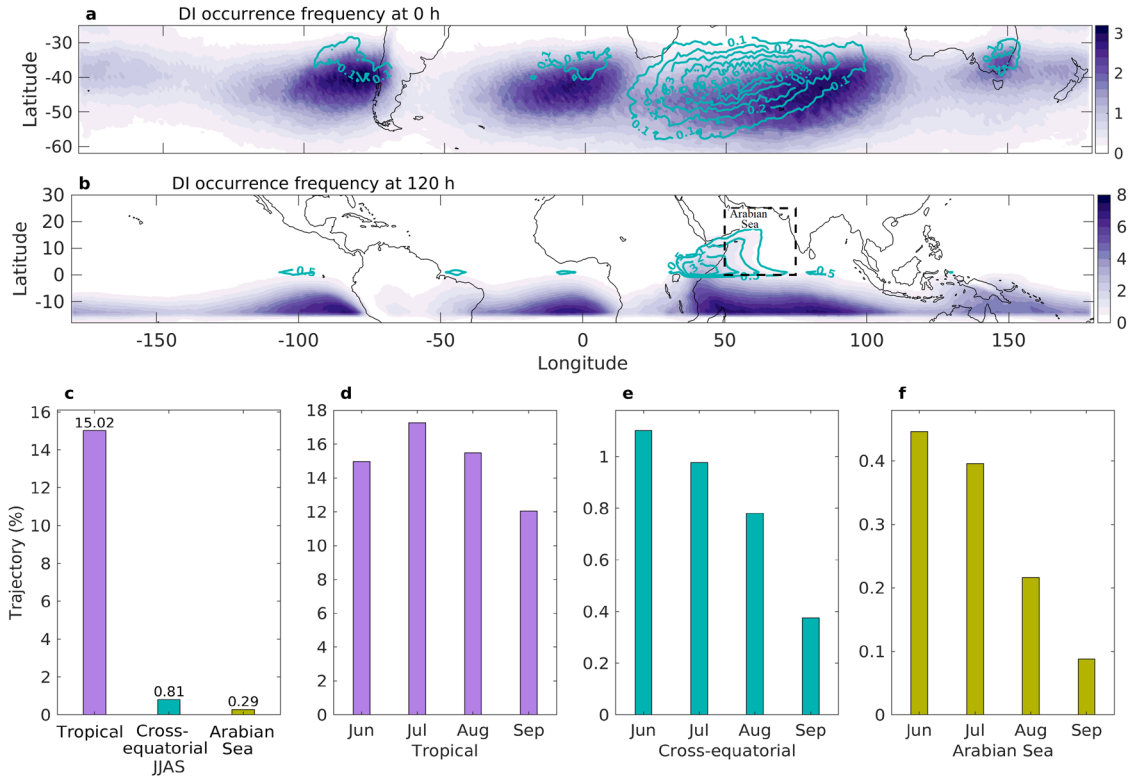

Fig. 2 Frequency of DI occurrence during JJAS. Geographical distribution of the fraction of 3-h time instances (%) at every 0.5° × 0.5° regular grid point when at least one DI was detected: Shown are tropical DIs that entered the tropics (15°S–15°N) after initiating outside this range (shaded), and cross-equatorial DIs that crossed the equator northward (cyan contours) at **a** 0 h, the initiation of their slantwise descent, and **b** 120 h from initiation of descent. The spacing between the cross-equatorial DI contours is 0.1–0.6 at 0.1 intervals for (**a**) and 0.5, 1, 2, and 3 for (**b**.) **c** The mean percentage of tropical, cross-equatorial, and Arabian Sea DIs, calculated with respect to the total number of DIs throughout the globe during the climatological period JJAS. Arabian Sea DIs are those that initiated in the southern hemisphere and reached the Arabian Sea box (dashed block in (**b**)). The percentage of **d** tropical, **e** cross-equatorial, and **f** Arabian Sea DIs, by month.

level wind, as can be seen in Fig. 3. However, a detailed investigation of this momentum transfer mechanism is yet to be clarified.

Following the Lagrangian evolution of the DI airmass, specific humidity increases 36 h into its descent (Fig. 6c), likely due to mixing with the moist boundary layer[29,34]. Locally over the CIO, the combination of intruding dry air and a stronger low-level wind triggers enhanced ocean evaporation (Fig. 3b, c, Figs. 6e and 7c). The transport of newly evaporated moisture from the CIO toward India significantly increases the moisture transport and total precipitable water (TPW) over the Arabian Sea following a DI event (Fig. 3b–d, Fig. 4b–d and Fig. 7d). Overall, enhanced wind speed and moisture transport in the Arabian Sea favor about 10–20% more transport of moisture toward the southern part India (Fig. 3b–d), compared to the seasonal climatology. After five days following t_e, as DI air covers the Arabian Sea, the anomaly patterns revert to the state when DIs are not present (hereafter 'no-DI') but with yet stronger wind speed and higher moisture content over the Arabian Sea than climatology (Fig. 3d).

The enhanced moisture transport is expected to result in increased precipitation downstream. Following DI events, the target region with intensified moisture transport indeed exhibits increased TPW and precipitation compared to climatology with positive precipitation anomalies throughout the target region within 5 days from t_e (Fig. 4b−d). The mean daily precipitation over the target region is enhanced by 17% following a DI (Fig. 5a and Table 1). About 3% increase in TPW accompanies this compared to climatology (Fig. 5b). The mean precipitation rates following DI events reach above 6.5 mm day^{-1}, compared to about 5.6 mm day^{-1} for the seasonal climatology (Fig. 5a). Further, the lower limit of both precipitation and TPW distributions are higher following DI events compared to their seasonal distribution (Fig. 5a, b). Hence, DI events are more likely to produce higher precipitation and TPW than climatology. In fact, localized extreme precipitation in the target region, exceeding 100 mm day^{-1} (e.g., Goswami et al.[10]), is embedded in 90% of the events, covering in each event an area of at least 1° × 1°. More extended areas of 40 or 100 grid points of 1° × 1° size experience extreme precipitation in over 41% or 17% of the events, respectively, within 5 days following t_e (not shown). Thus, extreme precipitation is common following DI events, with its spatial extent strongly varying among the cases.

To verify the connection between newly evaporated moisture from the CIO and precipitation or TPW over the target region, we conducted a lead-lag correlation analysis between every two sets of variables for the 6 days following each t_s (Fig. 5d, corresponding to DI events). For comparison, a similar analysis is done for 1096 time steps when no DI was present for 11 days before and after these time steps ('no-DI', Fig. 5c). It is evident that TPW and precipitation are positively correlated within the target region, reaching the highest correlation at zero lag, 0.57 during the no-DI condition and being even higher (0.92) after DI events (Fig. 5c, d). However, the connection of ocean evaporation over the CIO region with TPW and precipitation over the target region are very different for no-DI conditions and following DI events. The very weak correlation (<0.2) between the ocean evaporation and TPW when no DIs are present is replaced by above 0.8 from −72 to −48 h in the presence of DIs over the Arabian Sea (Fig. 5c, d). This indicates that ocean evaporation over the CIO precedes TPW in the target region by 48–72 h during DI events. Similarly, ocean

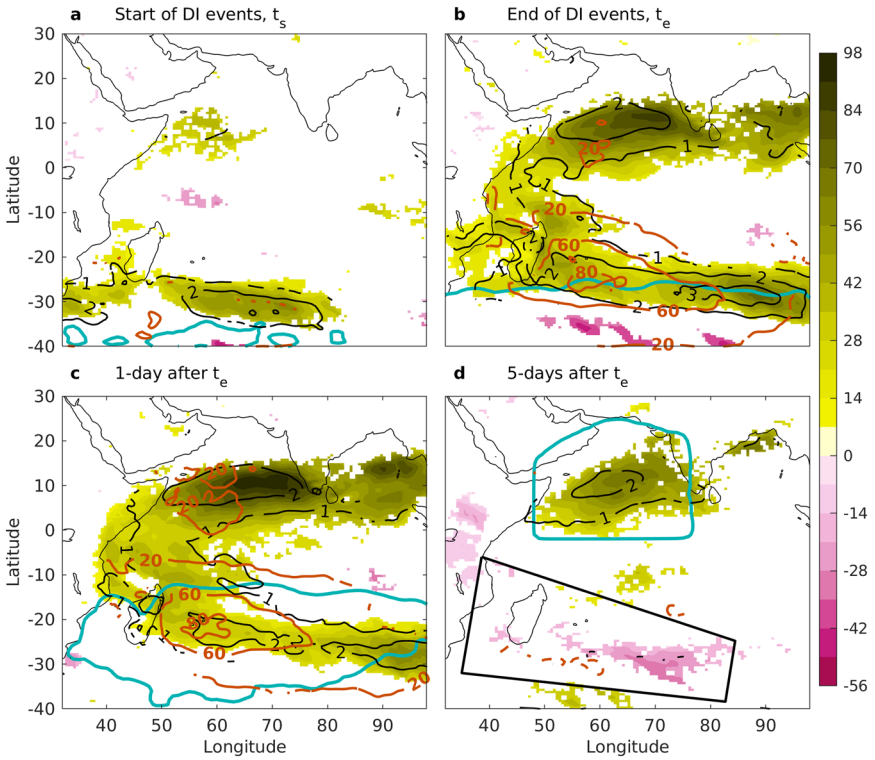

Fig. 3 Wind and moisture following DI events. Anomaly of wind speed at 850 hPa (m s^{-1}, black contours), ocean evaporation (W m^{-2}, orange contours), and moisture transport (integrated from the surface to 200 hPa, kg m^{-1} s^{-1}, shading) at **a** the start of a DI event, t_s, **b** end of a DI event, t_e, **c** 1 day after t_e, and **d** 5 days after t_e. Cyan contours represent a 0.01% occurrence frequency contour of Arabian Sea DIs during the corresponding stage in its lifetime. Dashed and solid contours represent negative and positive anomalies, respectively. All the anomaly fields shown are statistically significant ($P > 0.05$). The black box in **d** marks the area in the central Indian Ocean (CIO) with maximum ocean evaporation following t_e.

evaporation over the CIO leads to the highly-correlated variability in precipitation over the target region by 60 h or less (Fig. 5d). In other words, moisture from the CIO may take about 2–3 days to reach and precipitate over the target region under DI conditions. Hence, CIO, under a state of enhanced wind speed and ocean evaporation in the presence of DIs, becomes a significant moisture source for precipitation. Indeed, Athira et al.[15]. noted that during the Kerala flood of 2018, which is included in the 137 DI events, CIO moisture significantly contributed to the extreme precipitation. The active phase during 15–19 August 2018, which produced the catastrophic flood, was preceded by a DI event during 9–13 August 2018.

Lagrangian and Eulerian views of DI evolution

The characteristics of DI airmasses evolve from the initiation of their descent in the extratropical upper troposphere in the southern hemisphere (reference time 0 h) until they arrive at the marine boundary layer in the CIO. Examination of this Lagrangian evolution provides insight into the emergence of the moist anomalies in the CIO. By construction, DIs descend coherently more than 400 hPa within the initial 48 h, followed by a more gradual descent, reaching below 900 hPa by 120 h (Fig. 6a, black line). Overall, more than 75% of the DIs are below 800 hPa at 48 h. The increase in pressure along the trajectory indicates strong adiabatic warming. At the same time, however, the mean potential temperature during the first 48 h shows weak diabatic cooling from 304 to 298 K (Fig. 6b). The mean specific humidity increases continuously to 13 g kg^{-1} (Fig. 6c). Given that the humidity is almost zero, the diabatic cooling during the initial 18 h is likely due to radiative cooling. From 18 to 48 h, the increasing specific humidity (Fig. 6c) with increasing equivalent potential temperature (Fig. 6f) suggest that diabatic cooling can also be due to the evaporation of any liquid droplets as DIs mix into the relatively warm and moist boundary layer. Accordingly, relative humidity first decreases to its minimum during adiabatic descent (warming) from 0 to 18 h, while later, the increase in specific humidity dominates the enhancement in relative humidity, which remains high until 120 h (Fig. 6d).

A complementary perspective on the impact of DIs incoming into a given location can be gained from the Eulerian time series for anomalies of temperature at 850 hPa, specific humidity at 850 hPa, and ocean evaporation at the CIO (Fig. 7a–c). As DIs pass over the CIO region, their interaction with the marine boundary layer reduces the temperature by 0.7 K (Fig. 7a). Mixing dry air of the DIs with the moist boundary layer over the CIO induces a dry anomaly and thus enhances ocean evaporation by more than 40 W m^{-2} within the initial 12 h, due to an enhanced gradient in moisture and temperature between the surface and lower layers (Fig. 7a–c). The enhanced ocean evaporation raises the moisture content over the CIO region during the 36–48 h following t_e. The evaporation rate decreases with the moisture deficit decrease but nevertheless remains above the climatological mean (Fig. 7c). The robust moisture transport from the CIO region toward the Arabian Sea along the low-level jet does not allow a further increase in specific humidity (Fig. 7b); however, it does contribute to a more moist Indian subcontinent (Fig. 7d, e). Connecting the Lagrangian and Eulerian views, it is apparent that the intense ocean evaporation under DIs rapidly increases the specific humidity of the near-surface air and locally supplies moisture to the DI air. Therefore, the specific humidity further increases along the DIs, from 7 g kg^{-1} at 48 h to 13 g kg^{-1} at 120 h (Fig. 6c). Interestingly, ocean evaporation intensifies gradually at earlier times (Fig. 6e), likely due to associated extratropical

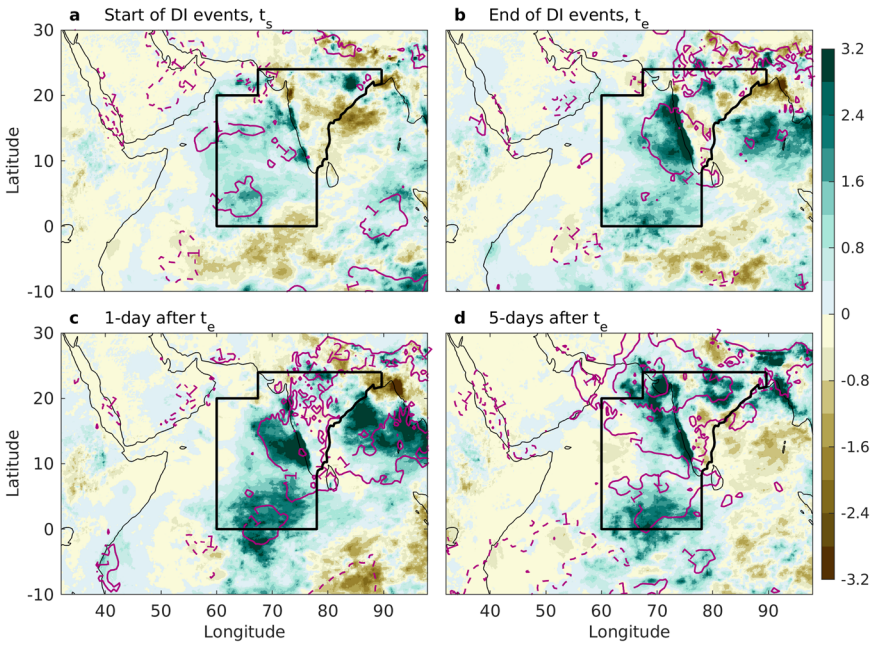

Fig. 4 Precipitation and TPW following DI events. a–d, Same as in Fig. 2 but for precipitation anomaly (mm day^{-1}, shading) and TPW anomaly (integrated from the surface to 200 hPa, mm, magenta contours). The black box in **a–d** is the target region associated with significant changes in precipitation and TPW over India and the Arabian Sea.

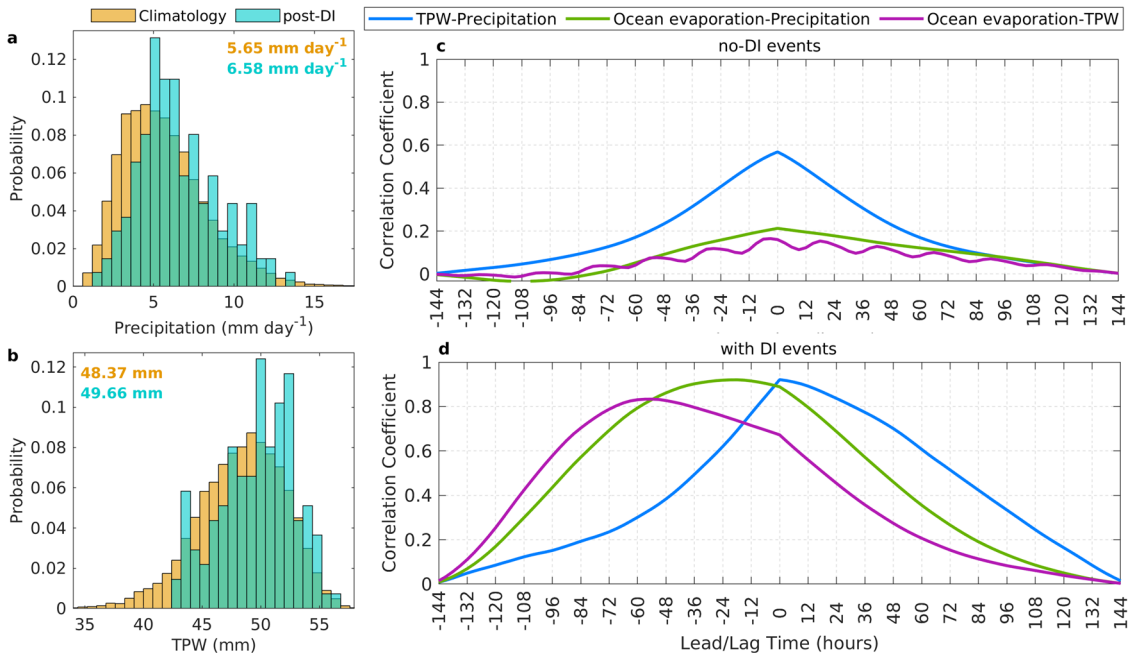

Fig. 5 Variability and correlation between TPW, ocean evaporation, and precipitation. a, **b** Histograms of the normalized frequencies of **a** precipitation and **b** TPW for the seasonal climatology (orange) and for 5 days after t_e (cyan). The numbers in color denote the mean during the respective category. **c**, **d** Lead-lag correlation between TPW–precipitation (blue line), ocean evaporation–precipitation (green lines), and ocean evaporation–TPW (magenta lines) for **c** a reference of no-DI conditions and **d** 6 days after t_s, i.e., following DI events. Precipitation and TPW are spatially averaged over the target region marked in Fig. 4, whereas ocean evaporation is spatially averaged over the CIO (black box in Fig. 3d).

systems[30,35,36]. However, the newly evaporated moisture before 36 h is not expected to increase the DI's specific humidity, as 95% of DIs are above 850 hPa at this stage. From 36 h onward, the interaction of DIs with the marine boundary layer triggers intense ocean evaporation, with the feedback also increasing the specific humidity.

Flavors of impact

Although the composite view in Figs. 3–7 and the synoptic conditions during the Kerala flood of 2018[15] are similar; the mean conditions for the 137 DI events are not always representative of individual events. According to Rodwell[32], the intrusion of dry, negative potential vorticity air from the southern hemisphere

Table 1. Mean precipitation (mm day^{-1}).

Mean precipitation	Land + ocean (target region marked in Fig. 4)	Land (marked yellow in Fig. 8d)
Climatological	5.65	7.07
All DI events	6.65 (+17.70%)	8.04 (+13.72%)
Cluster 1	8.19 (+44.96%)	11.21 (+58.56%)
Cluster 2	5.39 (−4.60 %)	6.66 (−5.80%)
Cluster 3	7.57 (+33.98%)	8.04 (+13.72%)
Cluster 4	5.19 (−8.14%)	5.86 (−17.11%)

Mean precipitation during t_e to $t_e + 5$ days is shown and is compared with the precipitation climatology during the summer monsoon season. The numbers in brackets denote the percentage change with respect to the seasonal climatological mean.

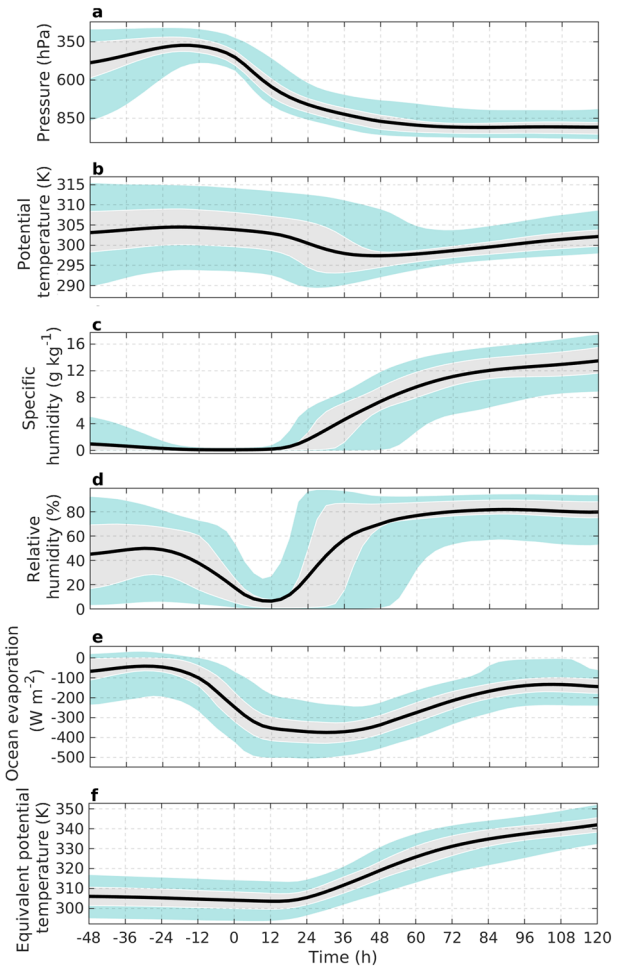

Fig. 6 Lagrangian time evolution of atmospheric variables along DI trajectories. Relative to the start of descent (0 h): **a** pressure level (hPa), **b** potential temperature (K), **c** specific humidity (g kg^{-1}), **d** relative humidity (%), **e** ocean evaporation (W m^{-2}), and **f** equivalent potential temperature (K). Note the atmospheric variables are traced along the three-dimensional location of the DI, while surface ocean evaporation (being a two-dimensional variable) is taken by considering the DI airmass horizontal location. The solid black line connects the mean from each time step, and the cyan and gray shadings represent the 5–95th and 25–75th percentile range, respectively. The coherent descent is diagnosed within the 0–48 h window, with an increase in pressure of more than 400 hPa.

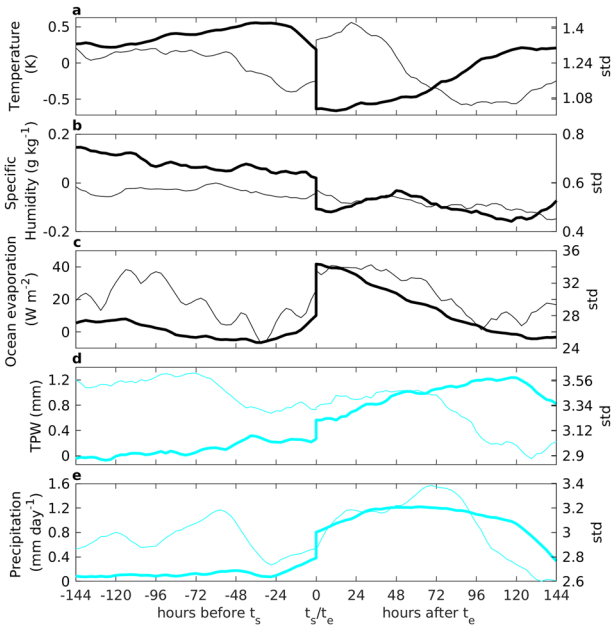

Fig. 7 Eulerian time evolution of atmospheric variables. Anomalies of **a** temperature at 850 hPa, **b** specific humidity at 850 hPa, **c** ocean evaporation (positive anomaly indicates more evaporation), **d** total precipitable water, TPW, vertically integrated between the surface and 200 hPa, and **e** precipitation before t_s and after t_e of DI events. The anomalies in **a**–**c** are spatially averaged within the CIO box shown in Fig. 3d. TPW and precipitation anomalies in **d**, **e** are averaged within the target region shown in Fig. 4. The left and right *y*-axis presents the mean absolute anomalies (bold line) and standard deviation (thin line) for the 137 events, respectively.

leads to a southward turning of the low-level flow and, therefore, to less rain over central and northwestern India. We examined the case-to-case flow variability and precipitation response, keeping the southward turning of the low-level flow in mind. To this end, we classified the 137 DI events into four groups based on wind speed anomaly at 850 hPa after five days following t_e, using a self-organizing map clustering algorithm (Fig. 8). The low-level wind over the Arabian Sea and India is stronger in clusters 1–3 and weaker in cluster 4 than climatology. Strong low-level jet favors more moisture transport and precipitation over India in clusters 1 and 3. In contrast, the weak low-level jet toward the Indian coasts in cluster 4 and the southern part of India in cluster 2 inhibits moisture transport and is associated with reduced rain over land (Fig. 8b, d). In cluster 3, stronger wind speed over the Arabian Sea is associated with high rain but is limited to the western Ghats with negative anomaly over land (Fig. 8c). Following Rodwell[32], due to more northward intrusion of air with negative potential vorticity, the anticyclonic turning of the low-level jet is more northward in cluster 1 than cluster 3 (Fig. 8a, c, Supplementary Fig. 3a, c). A stronger and northward-shifted low-level jet in cluster 1 brings more moisture along the west coast and towards the Indian monsoon region than in cluster 3 (Supplementary Fig. 3). Enhanced moisture transport facilitates more TPW and precipitation over India for cluster 1 (Table 1, Supplementary Fig. 4). However, the reason behind more northward wind speed for cluster 2, with the comparable latitudinal extent of negative potential vorticity as for cluster 3, is not clear, suggesting other contributing factors (Fig. 8b, c, Supplementary Fig. 3b, c).

The climatological progression of monsoon precipitation during JJAS adds another perspective to be considered. Most of India's rain occurs during July and August, such that negative seasonal anomalies in the monsoon core region prevail in June and September (Supplementary Fig. 5). Further,

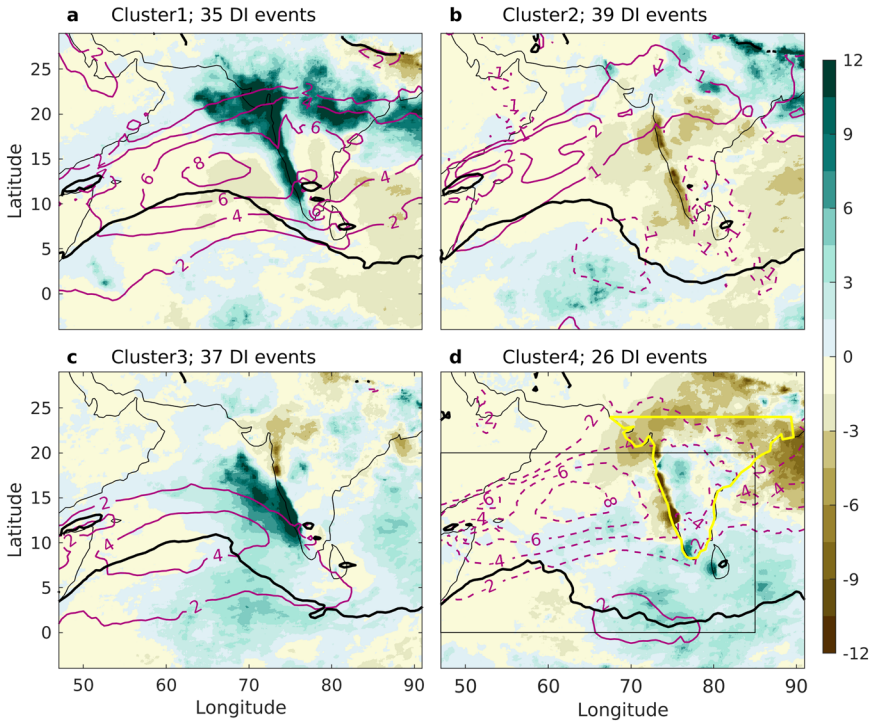

Fig. 8 Four clusters were identified using self-organizing map classification by wind speed anomaly at 850 hPa. The composite mean of wind speed anomaly at 850 hPa (m s^{-1}, magenta contours, solid for positive and dashed for negative), potential vorticity at 850 hPa (0 PVU; black contour, negative values are to its south), and precipitation anomaly in the fifth day following t_e (mm day^{-1}, shading) for **a** cluster 1, **b** cluster 2, **c** cluster 3, and **d** cluster 4. The black rectangle in **d** presents the area used for clustering, and the yellow line encloses the land fraction of the target area used in Table 1.

the precipitation anomalies along the west coast are strongly positive and negative during June and September, respectively (Supplementary Fig. 5a, d). A closer examination of each cluster reveals the existence of both positive and negative monthly precipitation anomalies (Supplementary Fig. 6). Based on the monthly variability, most DI events during July and August are associated with clusters 1–2, whereas clusters 3–4 mostly comprise events from June and September respectively (Supplementary Fig. 6). Hence the northward movement of monsoon during June to August and retreat in September has a clear impact on precipitation over India (Fig. 8, Supplementary Fig. 5). DIs, however, is associated with enhanced precipitation even during June and September (Supplementary Fig. 6c, d). Further, extremely heavy precipitation over the western part of India (near Gujrat) in cluster 1 cannot be ignored (Fig. 8a). Overall, in the presence of DI events, precipitation over land in India is enhanced by more than 13%, with about a 58% increase and 17% decrease for cluster 1 and cluster 4, respectively (Table 1).

DISCUSSION

This study reveals the crucial impact of episodic, cross-equatorial DIs on the Indian summer monsoon rainfall and its extremes by providing a Lagrangian-based 40-year climatology containing 137 DI events. The DIs studied here originate from the upper troposphere in the extratropical southern hemisphere, descend to the lower troposphere over the CIO, and finally reach the Arabian Sea within 5 days (Fig. 9a). Though rare (<1% of the global DIs and just over 3 events per season), DI events over the CIO are associated with the more intense low-level jet. Anomaly in the Indian summer monsoon rainfall during the days following DIs is summarized in Fig. 9. The DI airmasses are initially almost void of moisture, but upon reaching the boundary layer over the CIO (shading in Fig. 9b), they trigger intense ocean evaporation (>60 W m^{-2} above climatology) because of the moisture deficit at the air–sea interface and the strong wind speeds. Increased moisture uptake from the CIO due to the intensified low-level jet enhances moisture transport toward India. Thus, DIs create a positive anomaly of specific and relative humidity, as well as TPW, enhancing precipitation over the Indian region downstream. As a result of the modified moisture availability and transport over the target region following DIs, TPW increases by 3%, and precipitation increases by 17% on average. Further, out of 4 clusters comprising 137 events, cluster 1 is the stand-out flavor in terms of enhanced precipitation (+58% over land on average) and wind speed, with cluster 2 closer to cluster 3 and cluster 4 exhibiting reduced precipitation (−17% over land on average) and surface winds (Fig. 8, Table 1). Indeed, more than 55% of the break and active spells from 1979 to 2014 were preceded by such DI events (Supplementary Tables 1 and 2). From a mechanistic point of view, it is yet to be understood if and how the enhanced momentum of the low-level jet is related to the descending DI air. Moreover, detailed analysis based on individual cases is required to determine the relationship between the DI and the airmass, which finally precipitates over the target region—is it the same airmass?

In summary, the interaction of southern midlatitude systems with the moist marine boundary layer over the tropics enhances moisture transport and strongly modulates the summer monsoon rainfall, depending on the wind pattern often associated with its extremes. Prior knowledge of such interactions can improve the forecast of precipitation extremes during the Indian summer monsoon, given the potentially high predictability of extratropical weather. This knowledge is even more valuable for the assessment of flood-bearing rain extremes in a changing climate.

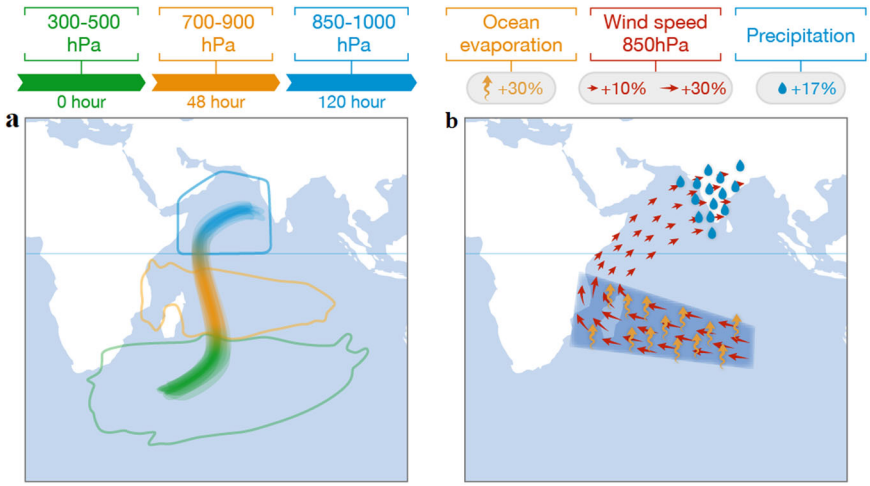

Fig. 9 Schematic summary of the anomalies following cross-equatorial DI events that reach the Arabian Sea. Progress and position, horizontally and vertically, of the dry intrusions are shown in **a**. Line contours present the horizontal progress of DIs relative to the initiation time of descent, i.e., 0 (green), 48 (orange), and 120 (cyan) hours respectively. The shaded trajectory represents the vertical position along a schematic example of a DI event for 120 h. The mean anomalies of ocean evaporation (orange arrows), wind speed at 850 hPa (red arrows), and precipitation (blue drops over India) during the days following DIs are shown in (**b**). The horizontal blue line marks the equator.

METHODS

Atmospheric data

All the atmospheric fields, except precipitation, are taken from the 5th reanalysis of the European Centre for Medium-Range Weather Forecasts (ERA-5)[37]. The ERA-5 data are interpolated to $0.5° \times 0.5°$ horizontal resolutions and 137 vertical hybrid levels at 3-h time intervals.

Precipitation data at high resolution ($0.1° \times 0.1°$ horizontal and 3-h temporal) are taken from Multi-Source Weighted-Ensemble Precipitation (MSWEP) version 2.8, which takes advantage of the complementary strengths of gauge, satellite, and reanalysis-based data to provide reliable precipitation estimates over the entire globe[38–40]. Precipitation from ERA-5 is highly correlated with MSWEP data over the target region (Supplementary Fig. 1). Overall, the data cover 40 Indian summer monsoon seasons (JJAS) from 1979 to 2018.

Identification of DIs

In general, DIs are defined as the slantwise descent of dry air parcels from the extratropical upper troposphere towards the lower troposphere in lower latitudes, often behind extratropical cyclones[41,42]. The slantwise descent is quasi-adiabatic, following the downward-sloping isentropes towards the equator[29]. The dryness of the air can potentially be expressed in terms of its water vapor content. However, humidity fields are highly sensitive to regional and seasonal variability. Considering this issue, Raveh-Rubin[29] established the descent-based Lagrangian criteria for DIs to avoid further complications related to moisture variability and obtained the degree of DI dryness as a result of the air descent rather than an assumption. In this study, the Lagrangian analysis tool LAGRANTO[43], driven by the time-varying three-dimensional wind fields from ERA-5, is used to identify DI airstreams. For each 3-h start time in JJAS, 1979–2018, DI trajectories are identified if the air parcels descend at least 400 hPa during the initial 48-h of their initiation above 600 hPa level, following Raveh-Rubin[29]. Extending the trajectories further until 120 h from their start of the descent, we label the trajectories as tropical, cross-equatorial, or Arabian Sea DIs. Tropical DIs are defined as DIs that entered the tropics (15°S–15°N) after initiating outside this range. The fraction of tropical DIs initiated in the southern hemisphere and crossed the equator while moving northward are defined as cross-equatorial DI. The cross-equatorial DIs reaching the Arabian Sea (Fig. 2b, dashed black block) are defined as the Arabian Sea DIs. Our study focuses on Arabian Sea DIs, which are hereafter termed 'DIs' for simplicity.

Definition of DI events

We consider a DI event to be a collection of DIs that initiate in consecutive time steps during a 3–120 h period. The time gap between the end of one DI event and the start of the next DI event is set to be at least 5 days (Eq. 1), meaning that DIs that occur within 5 days of each other are part of the same event, e.g., the first event in Supplementary Fig. 2. The start and end of DI event initiations are denoted by t_s and t_e, respectively, while n is the event number.

$$t_{s,n+1} - t_{e,n} \geq 5\,\text{days} \quad (1)$$

The additional 5-day gap criterion ensures we can examine the time-dependent influence of DIs on the downstream flow and humidity distribution without interference from other DIs (recall that each DI trajectory is tracked for 5 days). Additionally, to avoid noise caused by the presence of very few DIs, we require (i) that DI occurrence at a given time step is considered if at least 10 DIs are identified and (ii) each event lasts at least 6 h.

Based on the above criteria, 137 DI events were identified for the 40 summer monsoon seasons during 1979–2018, consisting of 110,062 DI trajectories that initiate during 1737 time steps, i.e., 4% of the time steps in JJAS.

Self-organizing map (SOM) classification algorithm

The self-organizing map (SOM), introduced by Kohonen in the 1980s, is an unsupervised neural network based on competitive learning[44]. This algorithm has been used in meteorological and climatic sciences since the late 1990s as a clustering and pattern recognition method[45]. Being trained using competitive learning rather than error-correction learning, the SOM has many advantages over conventional feature-extraction methods, such as principal component analysis or K-means methods. The SOM algorithm was successfully utilized to classify atmospheric flow patterns[45,46]. In this study, the SOM algorithm is used to understand the variability of the lower-tropospheric flow and its impact on the distribution of precipitation over India. The SOM

algorithm classified DI events based on the seasonal anomaly of 850-hPa wind speed in the Indian Ocean during the 5th day following t_e (Fig. 8d, black box). Four clusters exhibiting major differences in their mean wind anomalies are chosen in a 2-by-2 map configuration. Bigger configurations do not exhibit informative differences among the clusters.

DATA AVAILABILITY

ERA-5 data is freely available at https://cds.climate.copernicus.eu/#!/search?text=ERA5&type=dataset. MSWEP precipitation data can be downloaded at http://www.gloh2o.org/mswep/. Figures are produced with MATLAB (version 2020b). Lagrangian analysis tool LAGRANTO is used to calculate the trajectories. All data and codes in this paper are available upon request to Deepika Rai (deepika.rai@weizmann.ac.il).

Received: 21 September 2022; Accepted: 16 May 2023;
Published online: 26 May 2023

REFERENCES

1. Sahai, A. K., Grimm, A. M., Satyan, V. & Pant, G. B. Long-lead prediction of Indian summer monsoon rainfall from global SST evolution. *Clim. Dyn.* **20**, 855–863 (2003).
2. Parthasarathy, B., Munot, A. A. & Kothawale, D. R. All-India monthly and seasonal rainfall series: 1871-1993. *Theor. Appl. Climatol.* **49**, 217–224 (1994).
3. Saha, K. R., Mooley, D. A. & Saha, S. The Indian monsoon and its economic impact. *GeoJournal* **3**, 171–178 (1979).
4. Gadgil, S. & Gadgil, S. The Indian monsoon, GDP and agriculture. *Econ. Polit. Wkly.* **41**, 4887–4895 (2006).
5. Meehl, G. A. The annual cycle and interannual variability in the tropical pacific and indian ocean regions. *Mon. Weather Rev.* **115**, 27–50 (1987).
6. Goswami, B. N. & Ajaya Mohan, R. S. Intraseasonal oscillations and interannual variability of the Indian summer monsoon. *J. Clim.* **14**, 1180–1198 (2001).
7. Gadgil, S. The Indian monsoon and its variability. *Annu. Rev. Earth Planet. Sci.* **31**, 429–467 (2003).
8. Turner, A. G. & Annamalai, H. Climate change and the South Asian summer monsoon. *Nat. Clim. Chang.* **2**, 587–595 (2012).
9. Goswami, B. N., Chakraborty, D., Rajesh, P. V. & Mitra, A. Predictability of South-Asian monsoon rainfall beyond the legacy of Tropical Ocean Global Atmosphere program (TOGA). *Clim. Atmos. Sci.* **5**, 58 (2022).
10. Goswami, B. N., Venugopal, V., Sengupta, D., Madhusoodanan, M. S. & Xavier, P. K. Increasing trend of extreme rain events over india in a warming environment. *Science* **314**, 1442–1445 (2006).
11. Goswami, B. N. & Chakravorty, S. *Dynamics of the Indian Summer Monsoon Climate*. vol. 1 (Oxford University Press, 2017).
12. Rajeevan, M., Gadgil, S. & Bhate, J. Active and break spells of the Indian summer monsoon. *J. Earth Syst. Sci.* **119**, 229–247 (2010).
13. Gadgil, S. & Joseph, P. V. On breaks of the Indian monsoon. *Earth Planet. Sci.* **112**, 529–558 (2003).
14. Rao, T. N., Saikranthi, K., Radhakrishna, B. & Vijaya Bhaskara Rao, S. V. B. Differences in the climatological characteristics of precipitation between active and break spells of the Indian summer monsoon. *J. Clim.* **29**, 7797–7814 (2016).
15. Athira, U. N., Abhilash, S. & Ruchith, R. D. Role of unusual moisture transport across Equatorial Indian Ocean on the extreme rainfall event during Kerala flood 2018. *Dyn. Atmos. Ocean*. https://doi.org/10.1016/j.dynatmoce.2021.101225 (2021).
16. Vijaykumar, P. et al. Kerala floods in consecutive years—its association with mesoscale cloudburst and structural changes in monsoon clouds over the west coast of India. *Weather Clim. Extrem.* **33**, 100339 (2021).
17. Pathak, A., Ghosh, S., Alejandro Martinez, J., Dominguez, F. & Kumar, P. Role of oceanic and land moisture sources and transport in the seasonal and interannual variability of summer monsoon in India. *J. Clim.* **30**, 1839–1859 (2017).
18. Xavier, A., Kottayil, A., Mohanakumar, K. & Xavier, P. K. The role of monsoon low-level jet in modulating heavy rainfall events. *Int. J. Climatol.* **38**, e569–e576 (2018).
19. Findlater, J. A major low-level air current near the Indian Ocean during the northern summer. *Q. J. Roy. Meteor. Soc.* **95**, 362–380 (1969).
20. Roja Raman, M., Venkat Ratnam, M., Rajeevan, M., Jagannadha Rao, V. V. M. & Bhaskara Rao, S. V. Intriguing aspects of the monsoon low-level jet over peninsular India revealed by high-resolution GPS radiosonde observations. *J. Atmos. Sci.* **68**, 1413–1423 (2011).
21. Singh, D., Tsiang, M., Rajaratnam, B. & Diffenbaugh, N. S. Observed changes in extreme wet and dry spells during the South Asian summer monsoon season. *Nat. Clim. Chang.* **4**, 456–461 (2014).
22. Singh, R. & Sandeep, S. Dynamics of dry air intrusion over India during summer monsoon breaks. *Clim. Dyn.* **59**, 1649–1664 (2022).
23. Krishnan, R., Kumar, V., Sugi, M. & Yoshimura, J. Internal Feedbacks from Monsoon—midlatitude Interactions during Droughts in the Indian Summer Monsoon. *J. Atmos. Sci.* **66**, 553–578 (2009).
24. Krishnamurti, T. N., Thomas, A., Simon, A. & Kumar, V. Desert air incursions, an overlooked aspect, for the dry spells of the Indian summer monsoon. *J. Atmos. Sci.* **67**, 3423–3441 (2010).
25. Fadnavis, S. & Chattopadhyay, R. Linkages of subtropical stratospheric intraseasonal intrusions with Indian summer monsoon deficit rainfall. *J. Clim.* **30**, 5083–5095 (2017).
26. Roy, C., Fadnavis, S. & Sabin, T. P. The stratospheric ozone rich cold intrusion during El-Niño over the Indian region: implication during the Indian summer monsoon. *Int. J. Climatol.* **41**, E233–E248 (2021).
27. Parker, D. J. et al. The interaction of moist convection and mid-level dry air in the advance of the onset of the Indian monsoon. *Q. J. R. Meteorol. Soc.* **142**, 2256–2272 (2016).
28. Volonté, A., Turner, A. G. & Menon, A. Airmass analysis of the processes driving the progression of the Indian summer monsoon. *Q. J. R. Meteorol. Soc.* **146**, 2949–2980 (2020).
29. Raveh-Rubin, S. Dry intrusions: Lagrangian climatology and dynamical impact on the planetary boundary layer. *J. Clim.* **30**, 6661–6682 (2017).
30. Catto, J. L. & Raveh-Rubin, S. Climatology and dynamics of the link between dry intrusions and cold fronts during winter. Part I: global climatology. *Clim. Dyn.* **53**, 1873–1892 (2019).
31. Ramaswamy, C. & Pareek, R. S. The southwest monsoon over India and its teleconnections with the middle and upper tropospheric flow patterns over the Southern Hemisphere. *Tellus* **30**, 126–135 (1978).
32. Rodwell, M. J. Breaks in the Asian Monsoon: the influence of southern hemisphere weather systems. *J. Atmos. Sci.* **54**, 2597–2611 (1997).
33. Silverman, V., Nahum, S. & Raveh-Rubin, S. Predicting origins of coherent air mass trajectories using a neural network—the case of dry intrusions. *Meteorol. Appl.* **28**, 1–18 (2021).
34. Ilotoviz, E., Ghate, V. P. & Raveh-Rubin, S. The impact of slantwise descending dry intrusions on the marine boundary layer and air-sea interface over the ARM Eastern North Atlantic Site. *J. Geophys. Res. Atmos.* **126**, 1–24 (2021).
35. Papritz, L. et al. The role of extratropical cyclones and fronts for Southern Ocean freshwater fluxes. *J. Clim.* **27**, 6205–6224 (2014).
36. Aemisegger, F. & Papritz, L. A climatology of strong large-scale ocean evaporation events. Part I: Identification, global distribution, and associated climate conditions. *J. Clim.* **31**, 7287–7312 (2018).
37. Hersbach, H. et al. The ERA5 global reanalysis. *Q. J. R. Meteorol. Soc.* **146**, 1999–2049 (2020).
38. Beck, H. E. et al. MSWEP: 3-hourly 0.25° global gridded precipitation (1979-2015) by merging gauge, satellite, and reanalysis data. *Hydrol. Earth Syst. Sci.* **21**, 589–615 (2017).
39. Beck, H. E. et al. Global-scale evaluation of 22 precipitation datasets using gauge observations and hydrological modeling. *Adv. Glob. Chang. Res.* **21**, 6201–6217 (2017).
40. Beck, H. E. et al. MSWEP V2 Global 3-hourly 0.1° precipitation: methodology and quantitative assessment. *Bull. Am. Meteorol. Soc.* **100**, 473–500 (2019).
41. Wernli, B. H. A Lagrangian-based analysis of extratropical cyclones. II: a detailed case-study. *Q. J. R. Meteorol. Soc.* **123**, 1677–1706 (1997).
42. Browning, K. A. The dry intrusion perspective of extra-tropical cyclone development. *Meteorol. Appl.* **4**, 317–324 (1997).
43. Sprenger, M. & Wernli, H. The LAGRANTO Lagrangian analysis tool—version 2.0. *Geosci. Model Dev.* **8**, 2569–2586 (2015).
44. Kohonen, T. et al. *Self-Organizing Map*. (2001).
45. Liu, Y. & Weisberg, R. H. *A Review of Self-Organizing Map Applications in Meteorology and Oceanography, Self Organizing Maps—Applications and Novel Algorithm Design*. (ed Dr. Josphat Igadwa Mwasiagi, J. I.) (2011).
46. Givon, Y. et al. Large-scale drivers of the mistral wind: link to Rossby wave life cycles and seasonal variability. *Weather Clim. Dyn.* **2**, 609–630 (2021).

ACKNOWLEDGEMENTS

The Israel Meteorological Service and ECMWF are acknowledged for providing access to ERA-5 data. We thank Yonatan Givon, Leehi Magaritz-Ronen, Elody Fluck, Vered Silverman, and Erez Aviv (Weizmann Institute of Science) for the discussions, valuable suggestions, and technical help. This research is supported by the Israel Science Foundation (Grant No. 1347/18), the German-Israel Foundation (Grant No.: I-2525–307.8/2019) and the European Union (ERC, ExTrA, 101075826).

AUTHOR CONTRIBUTIONS

Conceptualization and investigation, writing-review and editing: D.R. and S.R-R. Writing-original draft, analysis, and visualization: D.R.., project administration and supervision: S.R-R.

COMPETING INTERESTS

The authors declare no competing interests.

ADDITIONAL INFORMATION

Supplementary information The online version contains supplementary material available at https://doi.org/10.1038/s41612-023-00374-7.

Correspondence and requests for materials should be addressed to Deepika Rai or Shira Raveh-Rubin.

Reprints and permission information is available at http://www.nature.com/reprints

Publisher's note Springer Nature remains neutral with regard to jurisdictional claims in published maps and institutional affiliations.